Article:

Yuan, R, Yu, HS, Hu, N et al. (1 more author) (2018) Non-coaxial soil model with an anisotropic yield criterion and its application to the analysis of strip footing problems. Computers and Geotechnics, 99. pp. 80-92. ISSN 0266-352X

https://doi.org/10.1016/j.compgeo.2018.02.022

Non-coaxial soil model with an anisotropic yield criterion and its application to the analysis of strip footing problems

Dr Ran Yuan

[1]Key Laboratory of Transportation Tunnel Engineering (Southwest Jiaotong University), Ministry of Education, Chengdu City, Sichuan Province,

610031, China

[2]State Key Laboratory for Geomechanics and Deep Underground Engineering, China University of Mining and Technology, Xuzhou City, Jiangsu Province, 221116, China

Email: yuanran@swjtu.edu.cn

Professor Hai-Sui YU

School of Civil Engineering,
University of Leeds, Leeds LS2 9JT, UK
Email: h.yu@leeds.ac.uk

Dr Nian Hu

Nottingham Centre for Geomechanics,

University of Nottingham, Nottingham NG7 2RD, UK

Email: greaterhu@163.com

Dr Yi He

Corresponding author

Faculty of Geosciences and Environmental Engineering

Southwest Jiaotong University, Chengdu City, Sichuan Province,

610031, China

Email: dell811@163.com

ABSTRACT

This paper presents numerical applications of a non-coaxial soil model, in which an anisotropic yield criterion is incorporated, to analyze two-dimensional strip-footing problems. Semi-analytical solutions of the bearing capacity for a strip footing that rests on anisotropic, weightless, cohesive-frictional soils are developed based on the slip line method. The degrees of influences of soil anisotropy and non-coaxiality on the bearing capacity of the strip footing are examined. From the viewpoint of strength and stiffness, it is necessary to incorporate both the strength anisotropy and non-coaxiality into numerical simulations and practical designs of geotechnical problems.

KEYWORDS: non-coaxial plasticity, soil anisotropy, numerical simulation, strip footing.

1. INTRODUCTION

Extensive experimental (e.g., [1-6]) and micromechanics-based (e.g., [7-11]) evidence has demonstrated that non-coaxiality, which refers to the non-coincidence of the principal axes of the stress and plastic strain rate tensors, is an intrinsic characteristic of granular materials. These fundamental insights have guided the development of numerous realistic continuum soil models. Approaches for constitutive modelling can be broadly classified into the phenomenological approach and the multi-scale approach for rate-independent elasto-plastic behaviors of granular materials under a quasi-static loading. The phenomenological approach directly describes the observed phenomena using an approximate and sophisticated mathematical formulation. In recent decades, a number of phenomenological models have been developed that consider the non-coaxial behavior of soils, and examples include the hypo-plastic models [12], the generalized sub-loading surface model [13]; among others ([14-16]). On the other hand, multi-scale approaches have been proposed to describe non-coaxial behavior of soils based on micro-mechanics. The macroscopic mechanical behavior of granular materials is then directly related to the evolution of the internal structure. One popular category within this framework can be classified as elasto-plastic models with fabric tensors (e.g., [17-19]).

However, analysis of practical geotechnical problems that consider the non-coaxial plasticity of granular soils is rare. Although phenomenological models have demonstrated their ability to capture many of the most salient features, e.g., dilatancy, soil anisotropy, hardening and strain localization, they often introduce too many parameters without physical meaning and are difficult to be calibrated. Indeed, the mathematical formulations for most of the current models based on phenomenological approaches are complex; hence, it is difficult for those non-coaxial models to be implemented into non-linear numerical codes for the solution of boundary value problems. With respect to the models that use multi-scale approaches, information on the evolution of the internal structure is difficult to define using the laboratory work. These reasons might explain why these non-coaxial constitutive models have not been widely applied to investigate boundary value problems.

Many real engineering problems subjected to proportional loading, e.g., tidal waves, earthquakes and footing-penetration, demonstrate obvious principal stress rotations [20-21]. It is accepted that the soil mass underneath a footing, especially in the vicinity of the footing edges, experiences a large amount of stress rotations under loading [22]. Yu and other authors [22, 23] numerically applied non-coaxial constitutive models to investigate shallow foundations. In these researchers' work, the application of non-coaxial models predicted a larger settlement prior to collapse compared with the conventional coaxial models. The conclusions drawn from this study clearly stated that without considering the non-coaxial behavior of soil, a high chance of unsafe design exists in shallow foundations. Nevertheless, work of the above researchers is restricted to soil strength isotropy. The natural characteristic of soils is anisotropic, and recent experimental observations have demonstrated that non-coaxiality is a significant aspect of soil anisotropy (e.g., [4]). As concluded by Tsutsumi and Hashiguchi [24], both the tangent effect (non-coaxiality) and the anisotropy in the yield condition must be incorporated into constitutive equations for a description of the general non-proportional loading behavior of soils. Assuming non-coaxiality in the context of soil isotropy might result in poor predictions of stability and serviceability problems in geotechnical engineering. Hence, it remains a key issue to gain insight into the different aspects that might be introduced into footing problems modeled by non-coaxial plasticity in the context of soil strength anisotropy compared with those that are modeled using coaxial plasticity.

In this paper, a plane-strain, elastic/perfectly plastic non-coaxial soil model with an anisotropic yield criterion is applied to simulate strip footing problems. The anisotropic yield criterion is generalized from the conventional isotropic Mohr-Coulomb yield criterion to account for the effects of initial strength anisotropy, which is characterized by the variation of internal friction angles (angles of shearing resistance) with the direction of the principal stresses. Based on the slip line method, a semi-analytical solution of the bearing capacity is presented for a strip footing that rests on an anisotropic, weightless, cohesive-frictional soil. Comparison between the numerical predictions and semi-analytical results of the bearing capacity are performed. The influences of degrees of soil anisotropy and non-coaxiality on the bearing capacity of strip footings are also discussed.

2. A NON-COAXIAL MODEL: DEVELOPMENT AND IMPLEMENTATION

The plane strain non-coaxial soil model used in this paper emphasizes on two ingredients: the anisotropic yield function and the non-coaxial plastic flow rule. The signs of the stress (rate) are chosen as positive for compression.

2.1 **The anisotropic yield criterion**

Following Booker and Davis [25], the anisotropic yield function in the stress space of $(\frac{\sigma_x-\sigma_y}{2}, \sigma_{xy})$ is a known function of the mean pressure p and the direction of principal stresses Θ. As shown in Fig. 1 and in line with the experimental evidence that the internal friction angle varies with the direction of principal stresses (e.g.,[4]), the yield criterion can be written as follows:

$$f(\sigma_x,\sigma_y,\sigma_{xy}) = R + F(p,\Theta) = 0 \tag{1}$$

where

$$F(p,\Theta) = (p - c\cdot\cot\phi_{max})\cdot\sin\phi(\Theta) \tag{2}$$

$$\sin\phi(\Theta) = \frac{n\cdot\sin\phi_{max}}{\sqrt{n^2\cos^2(2\Theta-2\beta)+\sin^2(2\Theta-2\beta)}} \tag{3}$$

and where $R = \frac{1}{2}[(\sigma_x - \sigma_y)^2 + 4\sigma_{xy}^2]^{1/2}$, p=$\frac{1}{2}(\sigma_x+\sigma_y)$, $\tan(2\Theta_p)=2\sigma_{xy}/(\sigma_x-\sigma_y)$, c denotes cohesion. The expression of Equation (3) is derived by geometric considerations.

As indicated in Fig. 1b, the cross-section of the anisotropic yield criterion is assumed to be a rotational ellipse. The centre of the anisotropic ellipse is assumed to be located at the original point O, and ϕ_{max} and ϕ_{min} are defined as the maximum and minimum peak internal friction angles, respectively along all possible major principal stress directions. The major and minor lengths of the ellipse depend on the maximum magnitudes of the peak internal friction angle, respectively. Two shape parameters n and β, as shown in Equation (3), are added to those material properties of the conventional isotropic Mohr-Coulomb yield criterion in order to define the anisotropic yield criterion:

- $n=\sin\phi_{min}/\sin\phi_{max}$, where the range of n is between 0 and 1. In particular, the isotropic Mohr-Coulomb yield criterion is recovered when n=1.0.
- β refers to an angle when the major principal stress (corresponding to the case of the maximum peak internal friction angle) is inclined to the deposition direction; and β ranges from 0 to $\frac{\pi}{4}$.

The two shape parameters can be obtained via tests using the hollow cylinder apparatus (HCA). Experimental investigations from the laboratory [4] can aid in testing the accuracy of the proposed anisotropic yield criterion, as illustrated in Fig. 2. The non-dimensional parameter b is the intermediate stress ratio defined as $b=(\sigma_2-\sigma_3)/(\sigma_1-\sigma_3)$. For a plane strain condition, b≈0.2-0.4.

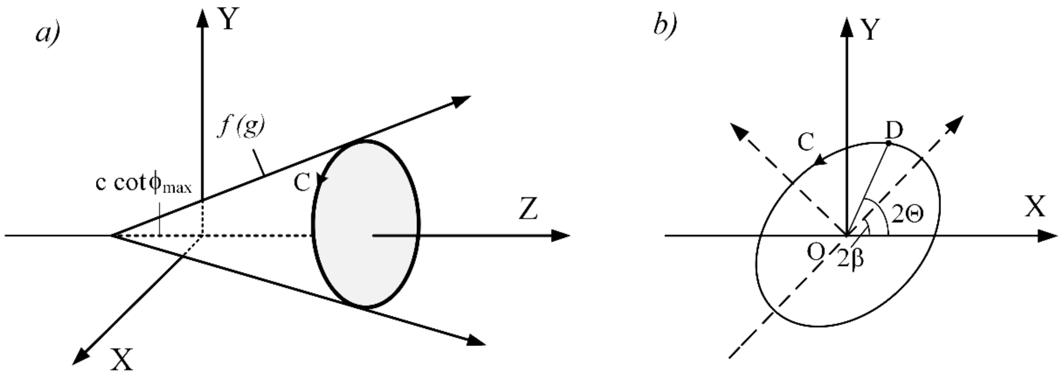

Fig. 1 Anisotropic yield surface in: (a) (X=$\frac{\sigma_x-\sigma_y}{2}$, Y=$\sigma_{xy}$, Z=$\frac{\sigma_x+\sigma_y}{2}$) space; (b) (X=$\frac{\sigma_x-\sigma_y}{2}$, Y=$\sigma_{xy}$) space.

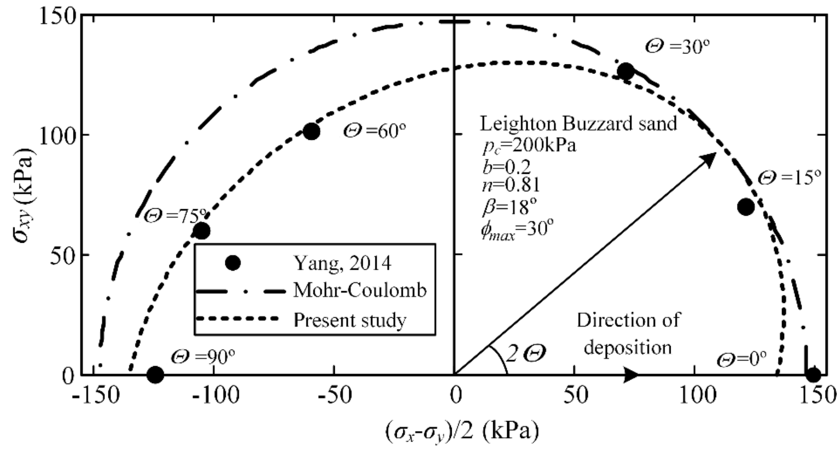

Fig. 2 Validation of the newly proposed anisotropic yield criterion.

2.2 The non-coaxial plastic flow rule

As indicated in Fig. 3, the general form of the plastic strain rate $\dot{\boldsymbol{\varepsilon}}^p$ consists of the conventional component $\dot{\boldsymbol{\varepsilon}}^{pc} = \dot{\lambda}\,\frac{\partial g}{\partial \boldsymbol{\sigma}}$ and the non-coaxial component $\dot{\boldsymbol{\varepsilon}}^{pt} = k \cdot \dot{\boldsymbol{T}}$. The conventional component is normal to the yield surface derived from the classical plastic potential theory. The non-coaxial component is tangential to the yield surface induced by the deviatoric stress-rate component. The general form of the plastic strain rate $\dot{\boldsymbol{\varepsilon}}^p$ is shown as follows:

$$\dot{\boldsymbol{\varepsilon}}^p = \dot{\lambda}\,\frac{\partial g}{\partial \boldsymbol{\sigma}} + k \cdot \dot{\boldsymbol{T}} \quad \text{if } f = 0 \text{ and } \dot{f} = 0 \tag{4}$$

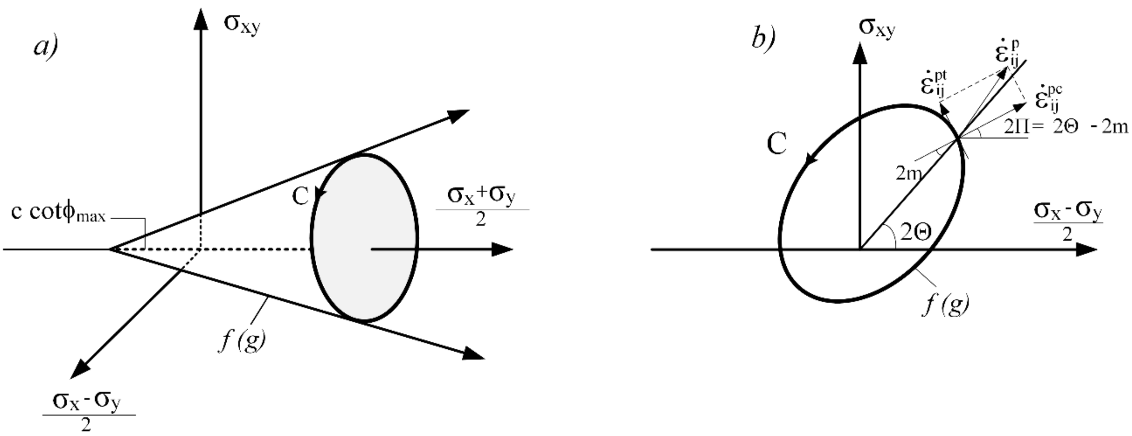

Fig. 3 Display of the non-coaxial plastic flow rule in: (a) (X=$\frac{\sigma_x-\sigma_y}{2}$, Y=$\sigma_{xy}$, Z=$\frac{\sigma_x+\sigma_y}{2}$) space; (b) (X=$\frac{\sigma_x-\sigma_y}{2}$, Y=$\sigma_{xy}$) space.

where $\dot{\lambda}$ denotes a positive scalar, g denotes the plastic potential, f represents the yield surface, k is a dimensionless scalar (known as the non-coaxial coefficient in this paper), and $\dot{\boldsymbol{T}}$ denotes the material derivative, which can be displayed in the form of principal stress increments:

$$\dot{\boldsymbol{T}} = \frac{1}{k} \cdot \boldsymbol{N} \cdot \boldsymbol{\sigma} \tag{5}$$

$\boldsymbol{N}$ is defined in Appendix 1.

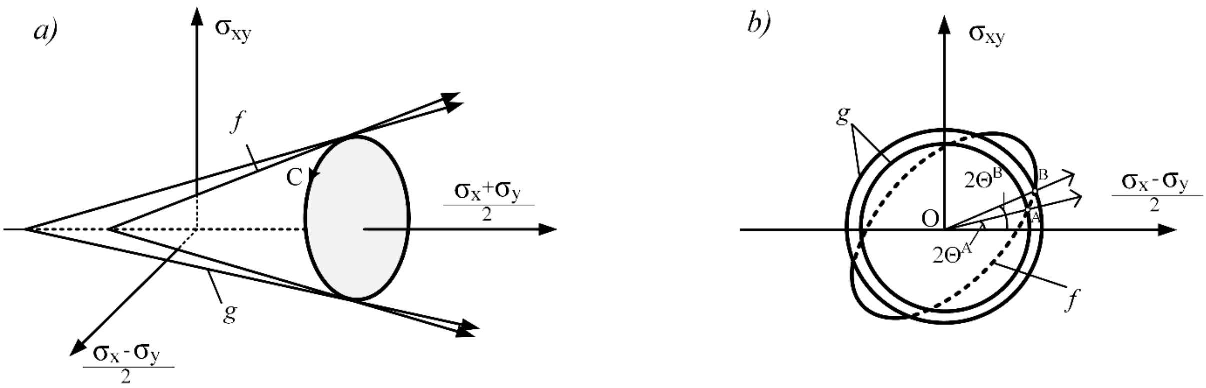

Fig. 4 Illustration of the plastic potential when the non-associativity in the conventional plastic flow rule is used in the space of: (a) (X=$\frac{\sigma_x-\sigma_y}{2}$, Y=$\sigma_{xy}$, Z=$\frac{\sigma_x+\sigma_y}{2}$); (b) (X=$\frac{\sigma_x-\sigma_y}{2}$, Y=$\sigma_{xy}$).

If g=f, then the associativity in the conventional plastic flow rule (abbreviated to asso) is used, and otherwise, the non-associativity in the conventional plastic flow rule (abbreviated to non-asso) is used. The plastic potential considers the effect of dilation angle. The dilation angle is assumed to vary with the direction of the principal stresses. As illustrated in Fig. 4, the plastic potential changes in size corresponding to different stress states (i.e., the plastic potential surface must pass the current point of the stress state). With this type of assumption, the conventional component is coaxial with the stress tensor. The form of g is shown with respect to the non-associativity in the conventional plastic flow rule is written as follows:

$$\mathrm{g} = \mathrm{R} + \mathrm{p} \cdot \sin\psi(\Theta) = \mathrm{C} \tag{6}$$

and

$$\sin\psi(\Theta) = \frac{\mathrm{n} \cdot \sin\psi_{\max}}{\sqrt{\mathrm{n}^2 \cos^2(2\Theta - 2\beta) + \sin^2(2\Theta - 2\beta)}} \tag{7}$$

where ψ_{max} denotes the maximum dilation angle and C denotes a constant.

Combining the elastic component in which Hooke's law is used, the general rate equation for an elasto-plastic relationship can be shown as follows:

$$\dot{\boldsymbol{\sigma}} = \boldsymbol{D}^{\boldsymbol{ep}} \dot{\boldsymbol{\varepsilon}} = \boldsymbol{D}^{\boldsymbol{e}} (\dot{\boldsymbol{\varepsilon}} - \dot{\boldsymbol{\lambda}} \frac{\partial \mathrm{g}}{\partial \boldsymbol{\sigma}} - \boldsymbol{N} \dot{\boldsymbol{\sigma}}) \tag{8}$$

where $\boldsymbol{D}^{\boldsymbol{ep}}$ denotes the elasto-plastic stiffness matrix, and $\boldsymbol{D}^{\boldsymbol{e}}$ denotes the elastic stiffness matrix. The consistency condition equation for perfect plasticity is written:

$$(\frac{\partial f}{\partial \boldsymbol{\sigma}})^T \cdot \dot{\boldsymbol{\sigma}} = 0 \tag{9}$$

Substituting $\dot{\boldsymbol{\sigma}}$ from Equation (8) into Equation (9), the expression of the scalar multiplier $\dot{\boldsymbol{\lambda}}$ can be obtained as follows:

$$\dot{\lambda} = \frac{\overline{\boldsymbol{D}^{\boldsymbol{e}}} (\frac{\partial f}{\partial \boldsymbol{\sigma}})^T \dot{\boldsymbol{\varepsilon}}}{(\frac{\partial f}{\partial \boldsymbol{\sigma}})^T \overline{\boldsymbol{D}^{\boldsymbol{e}}} \frac{\partial \mathrm{g}}{\partial \boldsymbol{\sigma}}} \tag{10}$$

in which a modified elastic stiffness matrix $\overline{\boldsymbol{D}^{\boldsymbol{e}}}$ is introduced as follows:

$$\overline{\boldsymbol{D}^{\boldsymbol{e}}} = (\boldsymbol{I} + \boldsymbol{D}^{\boldsymbol{e}} \boldsymbol{N})^{-\mathbf{1}} \boldsymbol{D}^{\boldsymbol{e}} \tag{11}$$

where $\boldsymbol{I}$ is the identity tensor.

The non-coaxial elasto-plastic stress-strain stiffness matrix is shown as follows:

$$\boldsymbol{D}^{\boldsymbol{ep}} = \frac{\overline{\boldsymbol{D}^{\boldsymbol{e}}}\frac{\partial g}{\partial \boldsymbol{\sigma}}\left(\frac{\partial f}{\partial \boldsymbol{\sigma}}\right)^{T}\overline{\boldsymbol{D}^{\boldsymbol{e}}}}{\left(\frac{\partial f}{\partial \boldsymbol{\sigma}}\right)^{T}\overline{\boldsymbol{D}^{\boldsymbol{e}}}\frac{\partial g}{\partial \boldsymbol{\sigma}}} \tag{12}$$

2.3 Implementation of the proposed model

The developed non-coaxial soil model was implemented in the ABAQUS finite element code via the user-defined material subroutine (UMAT). A hyperbolic approximation at the tip of the yield surface is used to eliminate singularity in which the anisotropic yield criterion is modified as follows [26]:

$$\mathrm{f}(\sigma_{\mathrm{x}},\sigma_{\mathrm{y}},\sigma_{\mathrm{xy}}) = \sqrt{\left(\frac{\sigma_{\mathrm{x}}-\sigma_{\mathrm{y}}}{2}\right)^2 + \sigma_{\mathrm{xy}}^2 + \mathrm{a}^2\sin^2\phi(\Theta)} - (\mathrm{p} + \mathrm{c}\cdot\cot\phi_{\mathrm{max}})\cdot\sin\phi(\Theta) \tag{13}$$

The original anisotropic yield function, i.e., Equations (1) - (3), is recovered if a is set to zero. As suggested by Abbo [26], the hyperbolic surface closely represents the anisotropic Mohr-Coulomb yield criterion when $a \leq 0.25\mathrm{c}\cdot\cot\phi$. The explicit integration algorithm (an explicit forward Euler/modified Euler pair) with automatic error controls that returns the stresses to the yield surface during the integration process is used to perform the numerical implementation [26]. The modified regula-falsi is used to solve the yield surface intersection problem. The flowchart for the implementation is displayed in Fig. 5.

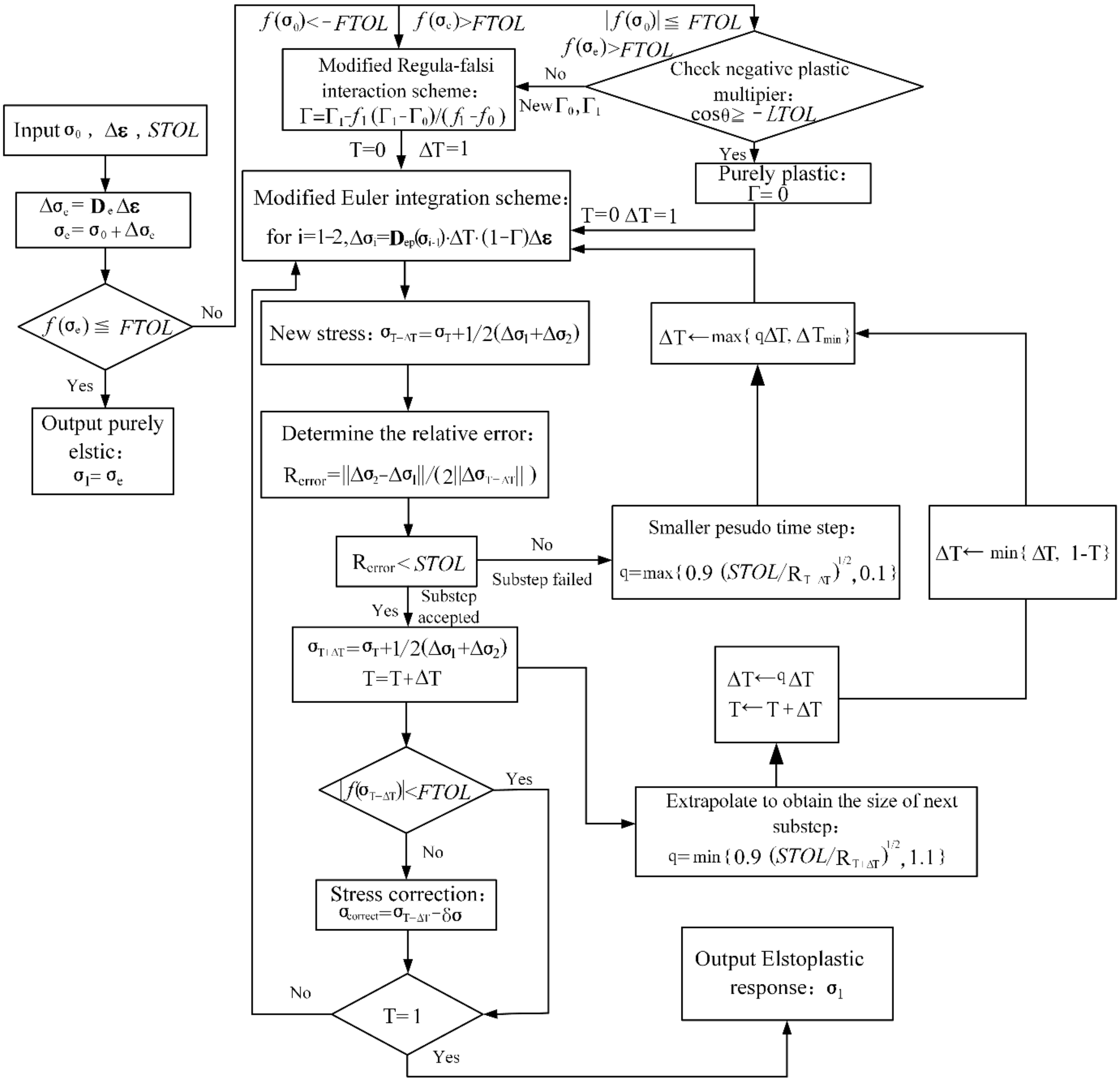

Fig. 5 Flowchart of the integration scheme

Fig. 6 shows the orientations of the principal stress and plastic strain rate in simple shear tests obtained using the newly proposed non-coaxial soil model. Obviously, the results ideally reproduce non-coaxial behaviors of the principal stress and the principal plastic strain rate.

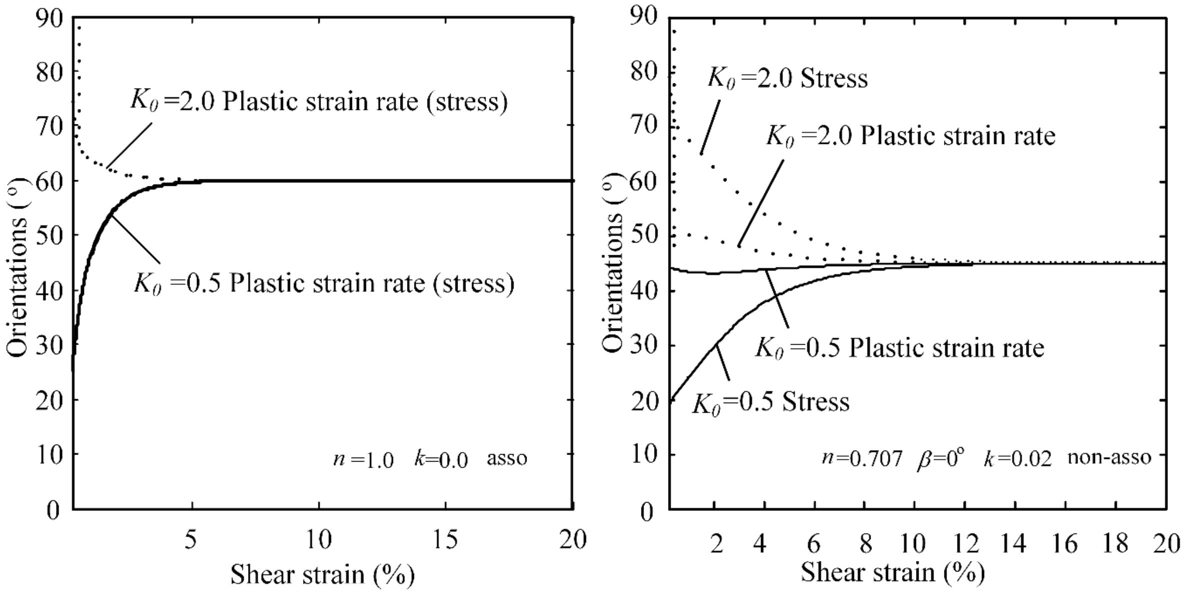

Fig. 6 Numerical simulation of simple shear problems in the condition of: (a) associativity and coaxiality; (2) non-associativity and non-coaxiality.

Particular attention should be focused on those cases in which severe non-coaxiality or non-associativity is used in the conventional plastic flow rule. For these situations, negative eigenvalues might be obtained in the solution of the global finite-element equations. For example, this scenario is especially prevalent for footing problems in which severe discontinuity of the stress field occurs in the vicinity of footing corners. Thus, to relax non-convergence problems in ABAQUS in these situations, the default force residual tolerance R_n=0.005 and the default displacement correction tolerance C_n=0.01 are adjusted to larger numbers (e.g., R_n=0.01 and C_n=0.05), which might reduce accuracy but within a tolerable range.

It should be noted that many findings in the literature have stated that the direction of the major principal stresses with respect to the x-axis lies on the interval (0,π/2) [4, 17]. Consequently, the anisotropic coefficient β should range within (0,π/4). In line with the previous experimental outcomes and to reduce parametric work, β is chosen as 0, 22.5° and 45° for discussion in this paper. Following the previous analyses [23], the non-coaxial coefficient k is chosen as 0, 0.02, and 0.1, to evaluate the effects of non-coaxial plasticity.

3. A SEMI-ANALYTICAL SOLUTION: ANISOTROPIC SOIL MASS

It is necessary to validate the numerical results with theoretical solutions to ascertain usability in practical, large-scale applications. To achieve this goal, semi-analytical solutions of the bearing capacity for a smooth strip footing resting on an anisotropic soil mass are developed based on the slip line method. For simplicity, a cohesive-frictional, weightless soil is considered for all analyses. Equations are presented in terms of stress fields, which must be satisfied in the plastic region of a rigid plastic body, and the magnitude of elastic strains is disregarded. The rigid plastic body is modeled using the anisotropic Mohr-Coulomb failure criterion, as shown in Section 2.1. The stress conditions on the boundary are illustrated in Fig. 7, where two families of characteristics can be introduced as (α, β) lines ([25, 27]):

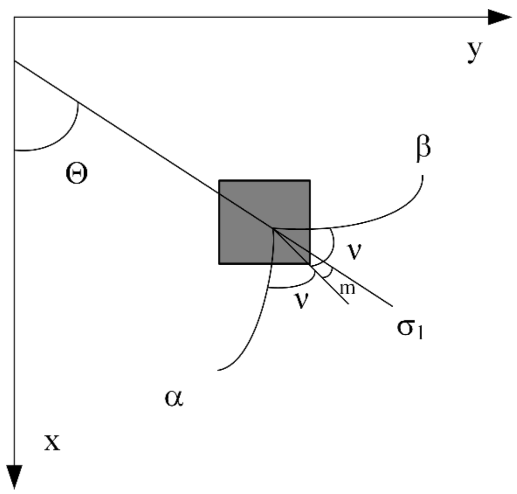

Fig. 7 Stress coordinate system and stress characteristics for anisotropic plasticity

$$\frac{dy}{dx} = \tan(\xi_\alpha) = \tan(\Theta - m - \nu) \tag{14}$$

$$\frac{dy}{dx} = \tan(\xi_\beta) = \tan(\Theta - m + \nu) \tag{15}$$

And,

$$\tan(2m) = \frac{1}{2F}\frac{\partial F}{\partial \Theta} \tag{16}$$

$$\cos(2\nu) = \cos(2m)\frac{\partial F}{\partial p} \tag{17}$$

where the variable m has a simple geometric interpretation and is introduced purely to ensure simplicity of the mathematics involved, and F is a function of p and Θ as shown in Equation (2).

The slip line method is illustrated in Fig. 8, where only a symmetrical footing problem is present. In this figure, AO is the half length of the strip footing, and a surface surcharge of q is applied on OB. Based on the corollary of Hencky's theory, all α-lines in this field must be straight lines, and all of these lines must pass through the edge point of the footing at O. The family of straight α-lines are the characteristics within the region COD that demonstrate an angle of Θ. By combining the equilibrium equations, if the stresses on the α-lines are integrated along the β-lines, the solution of vertical pressure at plastic collapse can be stated as follows:

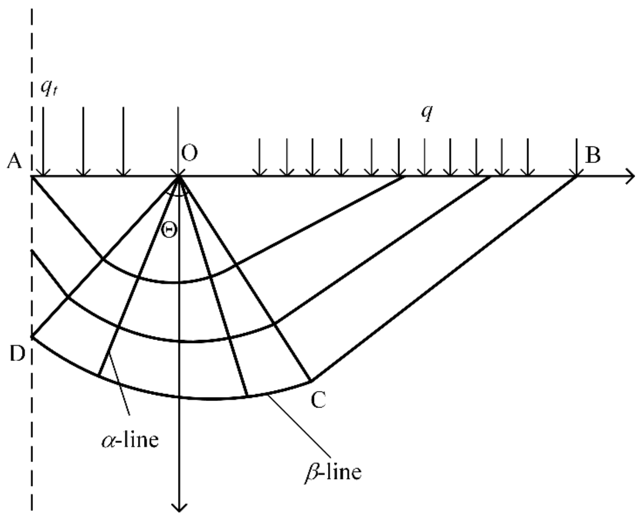

Fig. 8 Plastic stress field of strip footing with surcharge on OB.

$$q_t = (1+\sqrt{\frac{2}{M}}n\sin\phi_{max})(e^{\int_0^{\pi/2} G(\Theta)d\Theta} \cdot \frac{q\sqrt{M}+\sqrt{M}c\cot\phi_{max}}{\sqrt{M}-\sqrt{2}n\sin\phi_{max}}) - c\cot\phi_{max} \tag{18}$$

where G(Θ) and the detailed derivation are given in the Appendix 2, and $M = 2[(1-n^2)\sin^2(2\beta)+n^2]$. n and β are shape parameters, as illustrated in Section 2.1.

The above solution can be further expressed in terms of contributions from the cohesion (c) and surcharge (q) as follows:

$$q_t = N_c c + N_q q \tag{19}$$

where

$$N_c = (N_q - 1)\cdot \cot\phi_{max} \tag{20}$$

and

$$N_q = e^{\int_0^{\pi/2} G(\Theta)d\Theta} \cdot (1+\sqrt{\frac{2}{M}} n \sin\phi_{max}) \cdot \frac{\sqrt{M}}{\sqrt{M}-\sqrt{2} n \sin\phi_{max}} \tag{21}$$

In a special case in which a smooth strip footing rests on a purely cohesive soil mass without surface surcharge and the yield criterion is independent of hydrostatic pressure, i.e. $\upsilon = \frac{\pi}{4}$, the β-lines are circles. In this case, the yield surface is a cylinder generated by straight lines parallel to the line corresponding to $\sigma_x = \sigma_y$, $\tau_{xy} = 0$. The solution becomes much simpler and can readily be obtained analytically as follows:

$$q_t = \pi nc + 2(1-n)c + 2nc\sqrt{\frac{2}{M}} \tag{22}$$

In addition, for a special case of the Tresca model with $\phi = 0°$, the solution can be expressed in the following well-known form:

$$q_t = (2+\pi)\cdot c \tag{23}$$

which is consistent with Equation (22) when n=1.0.

As noted by Bishop [28], the stresses in the plastic stress solution have only been demonstrated to satisfy the yield condition and equilibrium equations in the plastic zone, and these stresses are referred to as a partial stress field or incomplete solutions. Such incomplete solutions are known as an upper bound solution (as developed in this paper). However, the bearing capacity obtained from the upper bound solution is quite similar to that of the exact solution. This solution has been generally applied to analyze current footing problems (e.g., [28]). In addition, the solutions proposed in this paper assume that an associated flow rule is valid. In this case, the stress and velocity characteristics are coincident such that the determination of a velocity field is not essential, which is the reason why the velocity field is not discussed in this paper.

In Equation (21), the integration of G (Θ), which is shown in the Appendix 2, is numerically performed in Matlab. A parametric study on the semi-analytical solution is conducted to investigate the influences of the anisotropic coefficients (i.e., shape parameters) n and β on the bearing capacity in terms of N_c and N_q. As shown in Fig. 9, it is evident that when the isotropic Mohr-Coulomb yield criterion is recovered (i.e., n=1.0), the bearing capacity obtained from the semi-analytical solution is identical to that obtained from Prandtl's solution. In general, the bearing capacity is lower when the yield surface is anisotropic compared with its isotropic counterpart. The predicted results of the bearing capacity increase with an increase in n but decrease with an increase in β. In addition, further validation can be demonstrated by comparing the semi-analytical solution of the bearing capacity N_c with the results from Cox [29], Spencer [30] and the method of limit analysis (after Chen [31]), as shown in Table 1. If the isotropic yield criterion is recovered when n=1.0, the results from those previous methods and the current semi-analytical solution are consistent with various internal friction angles. From the above analysis, it can be concluded that the strength of the soil is reduced when the soil yield anisotropy is considered. Hence, the predicted ultimate bearing capacity is much lower. This situation might result in an unsafe design for strip footing problems if the initial strength anisotropy is ignored.

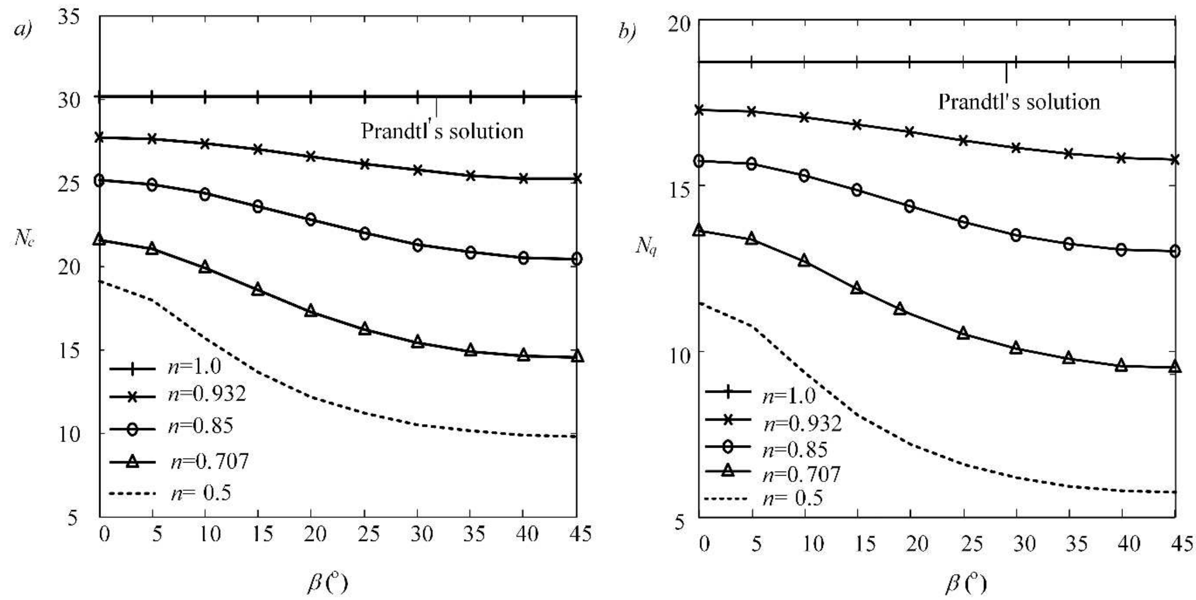

Fig. 9 Parametric study of the anisotropic coefficients ($\phi_{\max}$ =30°) : (a) N_c; (b) N_q.

Table 1 Variation of N_c with ϕ

ϕ (º)	Bearing capacity N_c				
	Cox (1962)	Spencer (1962)	Limit analysis (after Chen, 1975)	Semi-analytical solution	
				n=1.0	n=0.707 β=0º
10	8.34	8.35	8.35	8.35	7.27
20	14.8	14.8	14.8	14.8	11.99
30	30.1	30.1	30.1	30.1	21.48
40	75.3	75.3	75.3	75.3	43.18

4. NUMERICAL RESULTS AND DISCUSSION

A strip, rigid and smooth footing is assumed to rest on a weightless granular soil mass. Perfect plasticity is assumed for this case. The flow rule is associativity only for the comparison with semi-analytical results; otherwise, both associativity and non-associativity in the conventional flow rules are applied for numerical simulations performance to evaluate the effects of the flow rule.

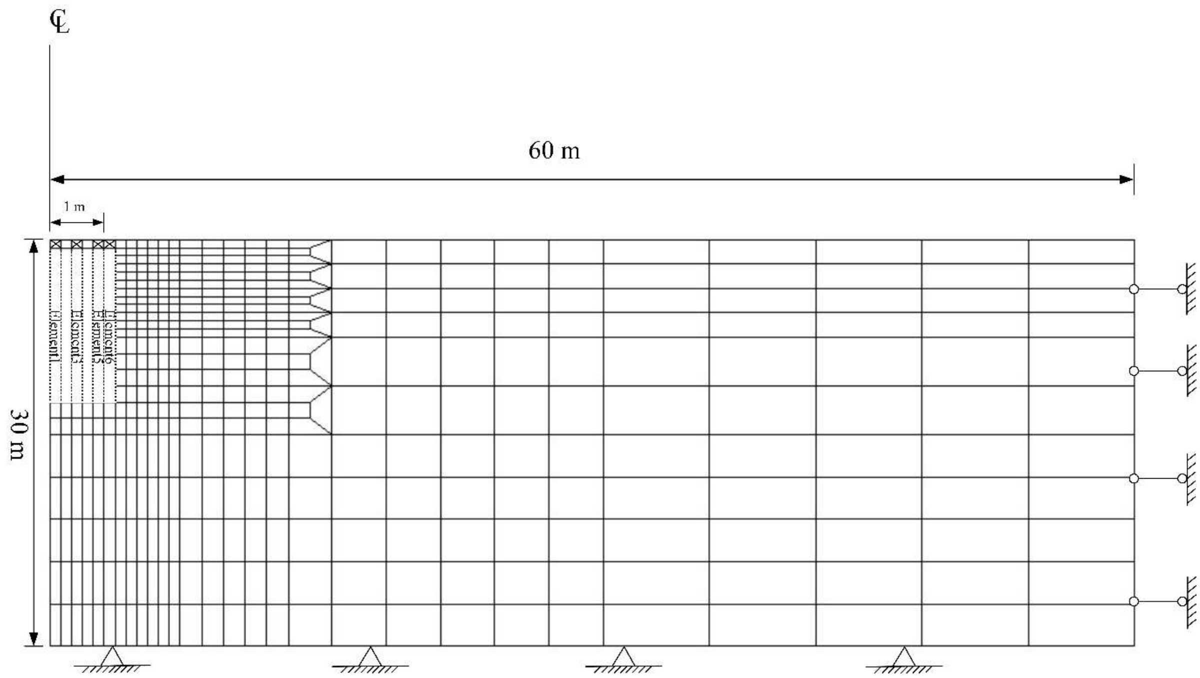

Fig. 10 Geometry and finite element discretization of the strip footing

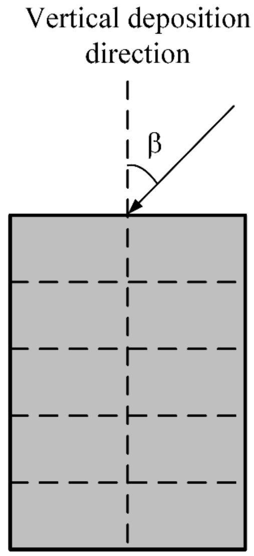

Fig. 11 Illustration of β

The model size for half of the base soil is assumed to be 60 m wide and 30 m deep, with the half width B of the footing set to 1 m. This negates the impact of the boundary conditions. The material of the base soil is discretized with first-order 8-node plane-strain reduced elements (element type CPE8R). The left-hand boundary represents a vertical symmetry axis, whereas the far-field condition on the right-hand side boundary allows for vertical movement. The condition on the bottom boundary is fixed in both the vertical and horizontal directions. The nodes immediately underneath the footing are free to move horizontally but are subject to the same amount of vertical downward movement. These nodes are subsequently applied in a gradually increasing, downward vertical displacement to simulate the movement of the footing. Two categories of simulations are performed: the first category has a footing located on a weightless cohesive-frictional soil without a surface surcharge, and the second category involves a footing located on a weightless cohesive-frictional soil with a 100 kPa surface surcharge. The maximum internal friction angle $\phi_{\max}$ is set as 30º, except in the analysis of the effect of varying $\phi_{\max}$ (eight values of $\phi_{\max}$ are applied from 5º to 40º at an interval of 5º) to validate the numerical results with semi-analytical results. Except for the analysis of a purely cohesionless soil, the cohesion c is set as 30 kPa. The typical elastic constants are fixed, i.e., Young's modulus $E = 10.0 \times 10^4$ kPa and Poisson's ratio $\upsilon = 0.3$. The shape parameter n defined in the anisotropic yield criterion represents the ratio of the minor axis over the major axis of the ellipse in the deviatoric space, relative to the magnitudes of the peak internal friction angle with the direction of principal stresses. The illustration of another shape parameter β relative to the deposition direction is shown in Fig. 11.

4.1 **Verification in terms of the bearing capacity**

The computation of the bearing capacity N_c, which is defined as the ultimate failure pressure normalized by the cohesion as obtained from the semi-analytical solution and numerical simulations with various internal friction angles, is illustrated in Fig. 12 a. The contributions of other bearing capacity factors are not taken into considerations, i.e., q=0 kPa. The footing is incrementally displaced immediately before the numerical convergence fails. For computation of the ultimate failure pressure normalized by the surface surcharge (q_t/q), as shown in Fig. 12 b, the cohesion is set as 30 kPa due to convergence problem for small friction angles. A good match of N_c and q_t/q can be observed between the numerical simulations and semi-analytical calculations for various anisotropic coefficients n and β. Generally, the numerical results deviate slightly further from the analytical results, but within a tolerable accuracy. The reasons for this outcome might lie in the presence of elasticity modeled by the elasto-plastic constitutive model in the numerical simulations, but for the semi-analytical solutions, the soil mass is modeled as a rigid, plastic body, and the elastic portion is ignored.

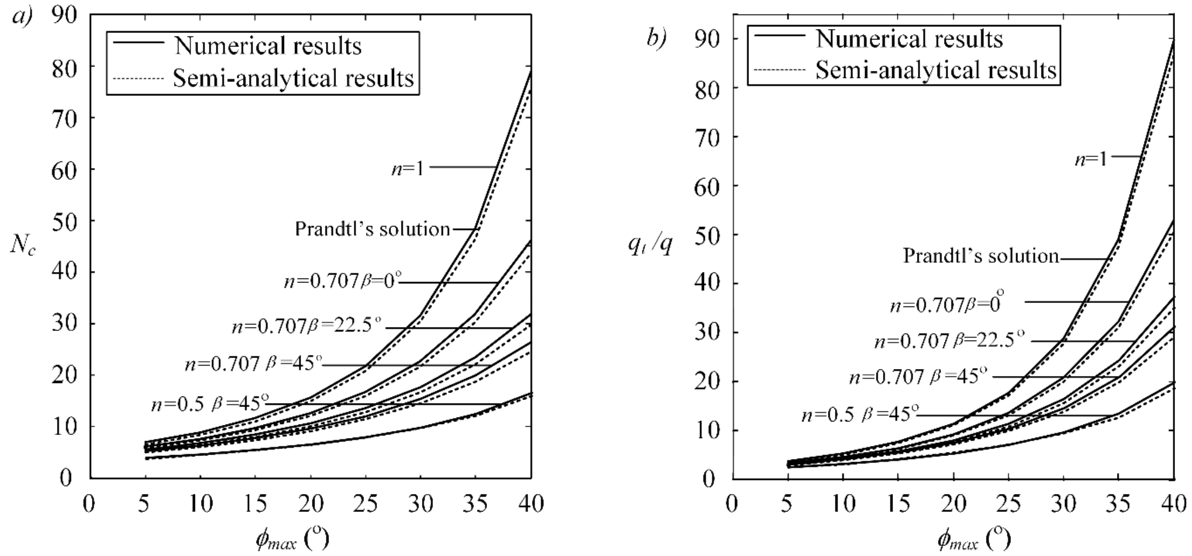

Fig. 12 Bearing capacity factors versus various internal friction angles: (a) N_c; (b) q_t/q.

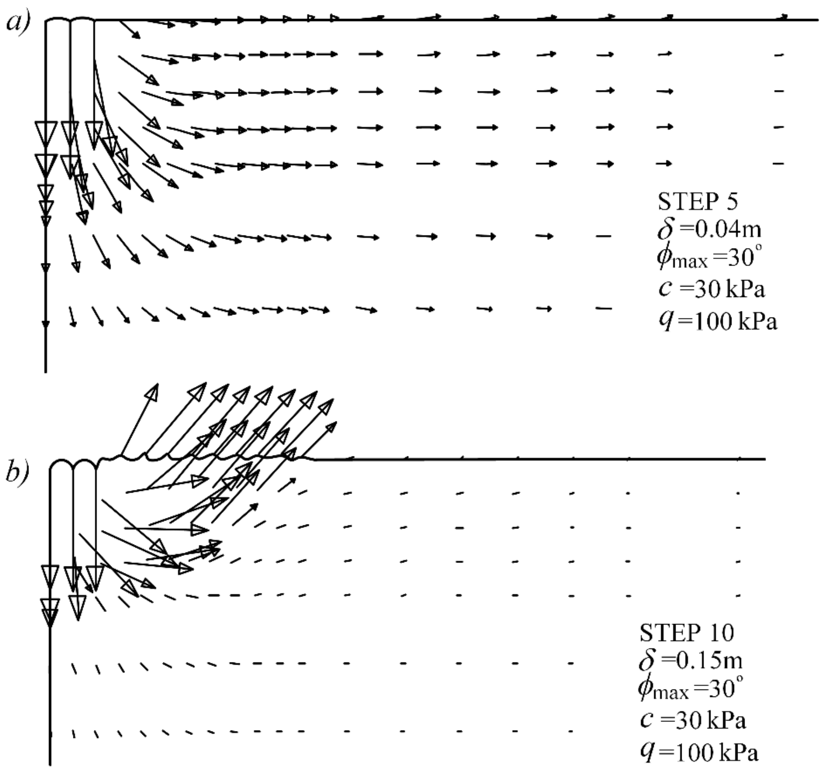

Fig. 13 The velocity field for the case of isotropic Mohr-Coulomb yield criterion for different steps of the computing in ABAQUS: a) fifth step; b) tenth step.

4.2 **Validation in terms of the velocity field**

Fig. 13 and Fig. 14 show the velocity fields obtained from the isotropic and anisotropic soils respectively. The directions of the arrows represent the flows of velocity. The scale of the magnitude of displacement, which is represented by the length of the arrow, is not identical. The exact magnitudes of the displacement are not given because they are not focused in the present study. The pattern of the black arrows visually indicate the β-lines compared with Fig.8. The velocity zone indicated by the anisotropic Mohr-Coulomb yield criterion (see Fig. 14) is larger and wider than that indicated by its isotropic counterpart (see Fig. 13). It can be expected that the failure zone is wider when the yield surface is anisotropic.

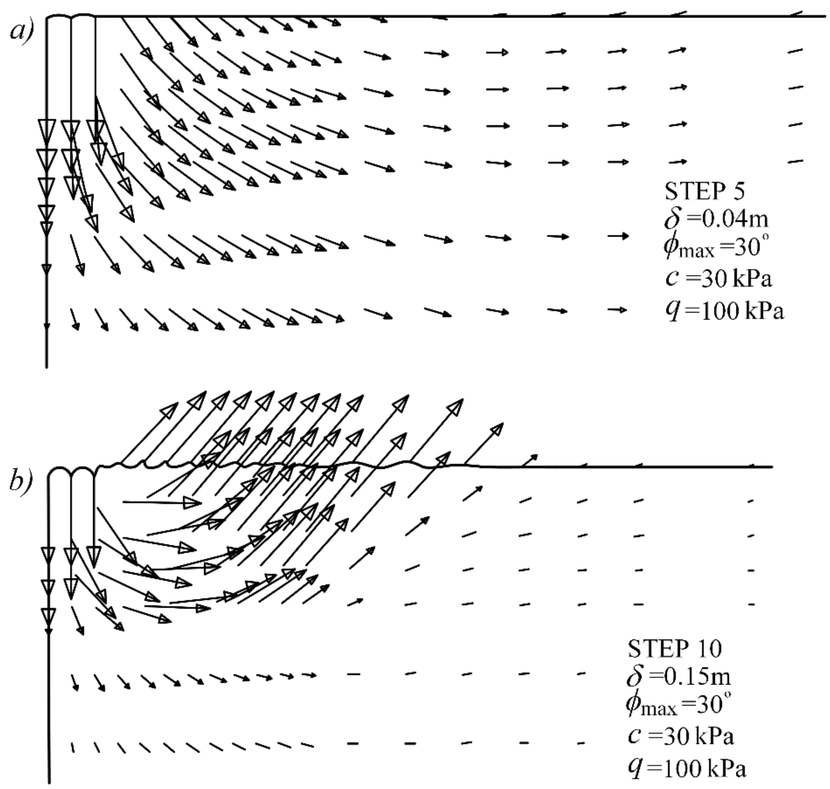

Fig. 14 The velocity field for the case of anisotropic Mohr-Coulomb yield criterion when n=0.707 and β=45^{o} , for different steps of the computing in ABAQUS: a) fifth step; b) tenth step.

4.3 **Evidence of principal stress rotations**

Four representative soil elements that are underneath and adjacent to the footings are highlighted in Fig. 10 with a black cross at the top. The stress paths of these representative elements are shown in Fig. 15. It is visually evident from these figures that these soil elements experience principal stress rotations.

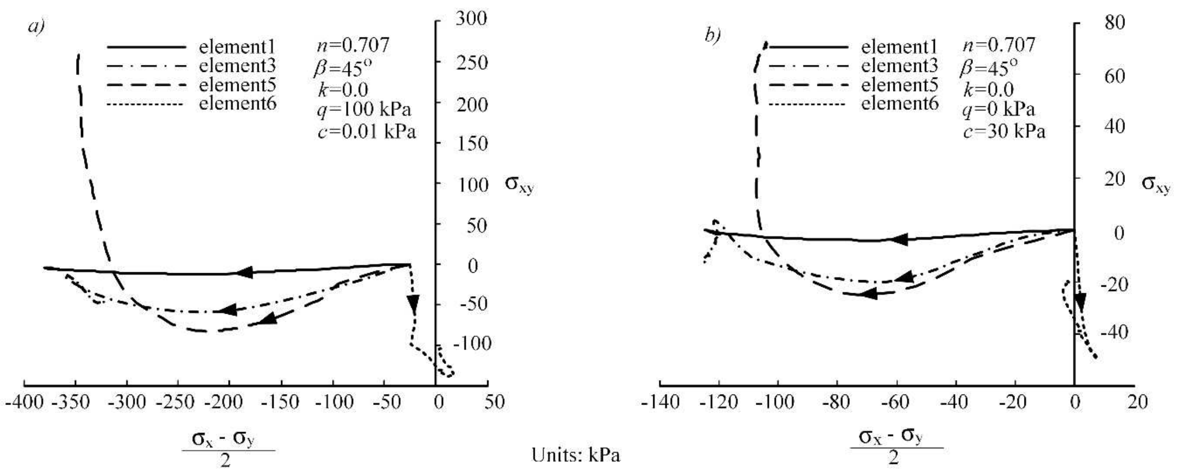

Fig. 15 Stress paths in the space of ($\frac{\sigma_x-\sigma_y}{2}$, σ_{xy}) from the numerical simulations: (a) computation of N_q; (b) computation of N_c.

4.4 **Influence of the degree of soil anisotropy and non-coaxiality on the bearing capacity due to the contribution of cohesion**

As shown in Equation (19), for computation of the bearing capacity N_c, contributions from other bearing capacity factors are neglected. The soil underneath the footing is assumed to be purely frictional-cohesive. The maximum internal friction angle is set as $\phi_{max} = 30^{\circ}$. When a non-associated condition is used, the dilation angle is set to $\psi_{max} = 20^{\circ}$ for computational convenience. The load-displacement curves are presented in Fig. 16 and Fig. 17. The vertical axis denotes the footing pressure normalized by cohesion (p/c), and the horizontal axis represents the displacement normalized by the half-width of the footing (Δ/B). The maximum difference of p/c prior to collapse between the coaxial (k=0.0) and non-coaxial predictions (k=0.1) is defined as follows (as illustrated in Fig. 16):

$$R_r = \frac{N_c(k=0.0) - N_c(k=0.1)}{N_c(k=0.0)} \tag{24}$$

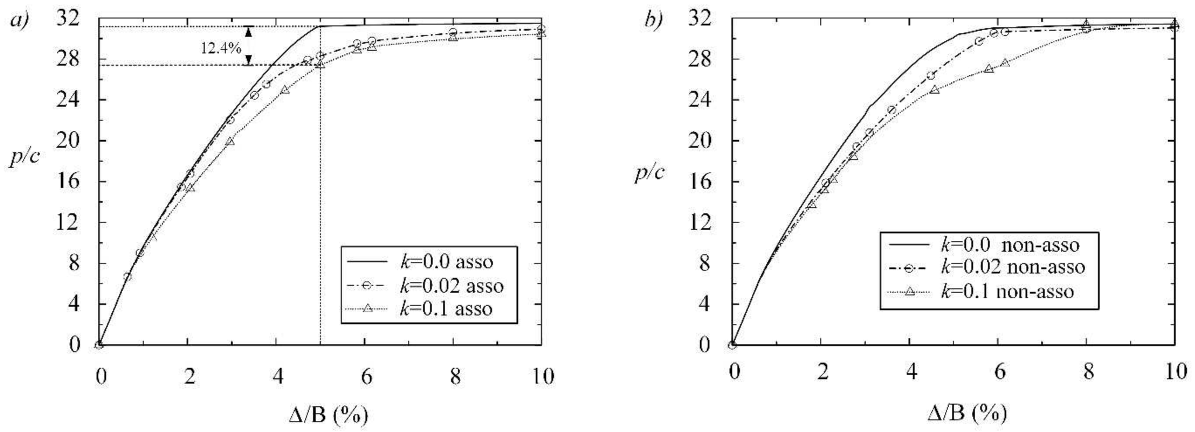

Fig. 16 Load-displacement curves of the bearing capacity N_c when the isotropic Mohr-Coulomb yield criterion is recovered (n=1.0): (a) associativity; (b) non-associativity.

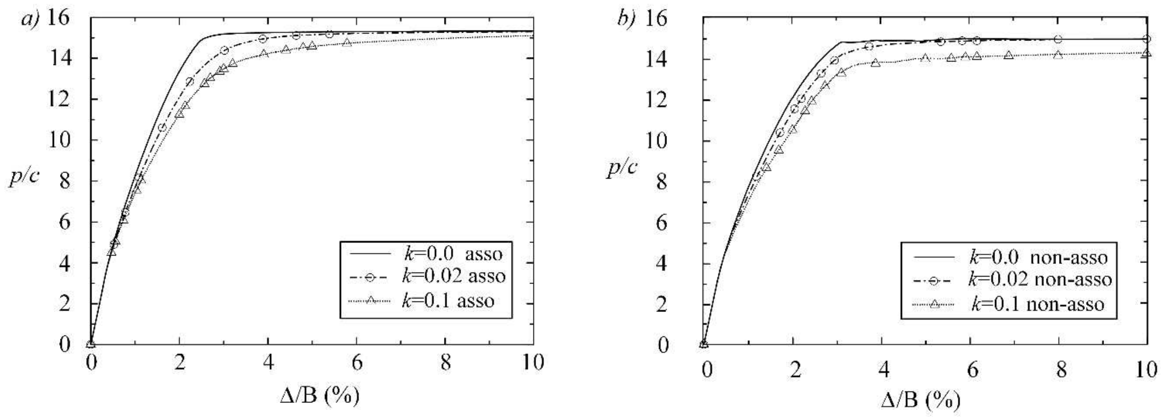

Fig. 17 Load-displacement curves when n=0.707 and β=45°: (a) associativity; (b) non-associativity.

As shown in Fig. 16, when the shape parameter n=1.0, i.e., the isotropic Mohr-Coulomb yield criterion, is recovered, the ultimate failure is reached at a normalised displacement Δ/B around 5%-6%. The settlement prior to collapse is larger when the non-coaxial coefficient is not equal to zero. The settlement increases with an increase in the non-coaxial coefficient k. It can be concluded that the soil is softened when non-coaxial plasticity is present. However, the ultimate bearing capacity N_c is not significantly affected and tend to be identical when approaching a large displacement for various values of k. As illustrated in Fig. 17, for the anisotropic case, the ultimate failure is reached at around Δ/B = 2.3% and Δ/B = 3% for the associativity and non-associativity in the conventional flow rules, respectively. When compared Fig.16 and Fig.17, the soil strength anisotropy exhibits a significant impact on the strength of the soil mass. The results show that the exclusion of initial soil strength anisotropy tends to delay the onset of the ultimate bearing capacity.

The parametric study is presented in Table 2. The results indicate that the onset of the ultimate bearing capacity and the maximum difference R_r depend on the degree of initial strength anisotropy and non-coaxiality. Conclusions can be drawn that the influence of the use of associativity/non-associativity is insignificant. For particular cases (e.g., Test5), the results from non-coaxial modelling for k=0.1 match closely with those from coaxial modeling for k=0.0. The most influenced case occurs for n=0.85 and β=45° (Test2). The stiffness of soil mass prior to failure is definitely influenced by the degree of non-coaxiality, whereas the effects of non-coaxiality on the bearing capacity are influenced by soil yield anisotropy, but the ultimate bearing capacity is not significantly affected.

Table 2 Maximum difference R_r for the computation of N_c.

	n	β(°)	Asso/Non-asso	Δ/B (%)	R_r(%)
Test1	1.0	N/A	Asso	5	12.4
			Non-asso	6	13.1
Test2	0.85	45	Asso	3.4	**13.5**
Test3	0.707	45	Asso	2.3	10.9
			Non-asso	3	10.0
Test4	0.707	22.5	Nsso	3	6.8
			Non-asso	2.8	6.8
Test5	0.707	0	Asso	4.3	**4.6**
			Non-asso	5.3	4.9

4.5 Influence of soil anisotropy and non-coaxiality on the bearing capacity due to the contribution of surface surcharge

A uniform surface surcharge of 100 kPa is applied for computation of bearing capacity N_q. The cohesion is set to c=0.01 for convergence convenience. The maximum internal friction angle is set as $\phi_{max} = 30^{\circ}$. When a non-associativity in the conventional flow rule is used, the dilation angle is set as $\psi_{max} = 20^{\circ}$ for computational convenience. The coefficient of earth pressure at rest, i.e. K_0, are assumed as 0.5 and 2.0. Both associativity/non-associativity in the conventional flow rules are used in this instance. The vertical axis denotes the footing pressure normalized by the surface surcharge (p/q), and the horizontal axis represents the displacement normalized by the half-width of the footing (Δ/B). The maximum difference of p/q prior to collapse between the coaxial (k=0.0) and non-coaxial predictions (k=0.1) is defined as follows:

$$R_s = \frac{N_q(k=0.0) - N_q(k=0.1)}{N_q(k=0.0)} \tag{25}$$

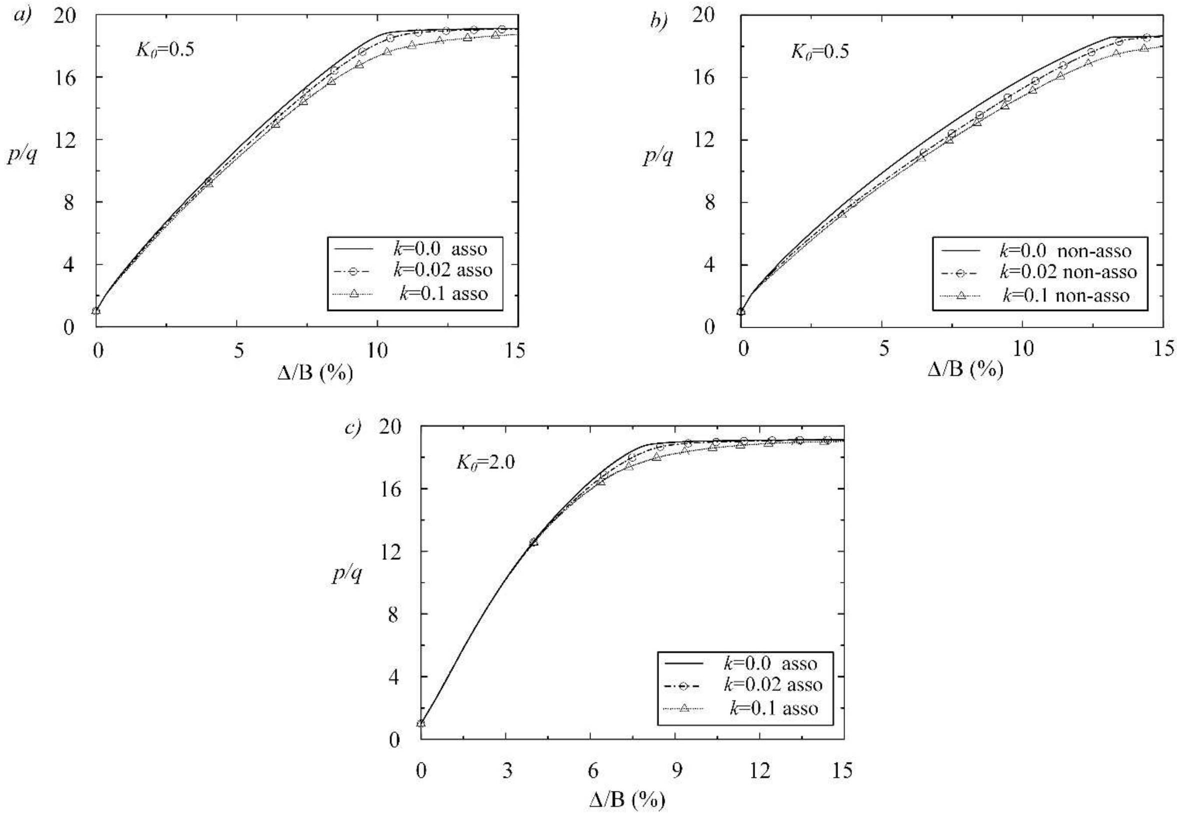

Fig. 18 Load-displacement curves of the bearing capacity N_q when the isotropic Mohr-Coulomb yield criterion is recovered (n=1.0): (a) lateral stress ratio K_0=0.5 and associativity; (b) lateral stress ratio K_0=0.5 and non-associativity; (c) lateral stress ratio K_0=2.0 and associativity.

Fig. 18 and Fig. 19 show the pressure-displacement curves obtained from the isotropic and anisotropic modelling, respectively. Non-coaxial modelling affects the settlement prior to collapse, which indicates that the soil is softened. In this scenario, the results indicate that the maximum difference R_s, which can account for the influence of non-coaxiality on the stiffness of soil mass prior to failure, depends on the lateral stress ratio, degree of initial strength anisotropy and flow rule. The ultimate value of the bearing capacity N_q is rarely affected by the introduction of non-coaxial plasticity. However, the ultimate bearing capacity is reached with $\frac{\Delta}{B} = 6\%$ when the yield strength anisotropy is applied (Fig. 19 a), which is nearly half of that with $\frac{\Delta}{B} = 10.5\%$ when its isotropic counterpart is applied (Fig. 18 a). Generally, a similar phenomenon is obtained as compared with that due to the contribution of cohesion. However, the influences of non-coaxiality and initial strength anisotropy are pronounced when compared with those of the bearing capacity due to the contribution of cohesion, as shown in Figure 19. A parametric study with respect to different values of lateral stress ratio, anisotropic coefficients (n and β), non-coaxial coefficient (k) and flow rules is shown in Table 3. For a value of K_0 of 2.0, few differences exist between the coaxial and non-coaxial predictions, for which the minimum of R_s can be 4.6%. The maximum difference R_s increases with a decrease in the value of n. However, when comparing Tests 8, 9 and 10, the maximum difference R_s sharply decreases with smaller values of β. The value drops from a maximum of R_s=28.3% to a minimum of R_s=3.4% for such a scenario. Hence, the effects of two shape parameters from the anisotropic yield criterion on R_s are highly evident.

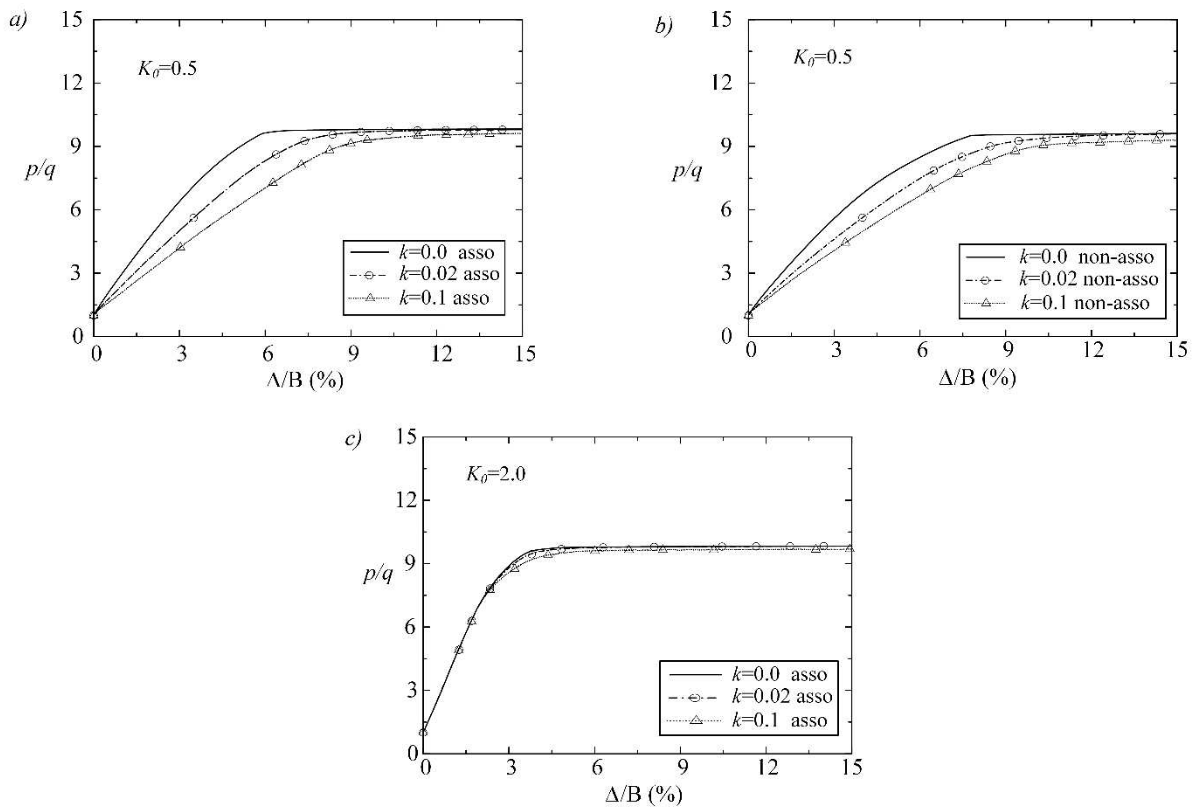

Fig. 19 Load-displacement curves of the bearing capacity N_q when n=0.707 and β=45°: (a) lateral stress ratio K_0=0.5 and associativity; (b) lateral stress ratio K_0=0.5 and non-associativity; (c) lateral stress ratio K_0=2.0 and associativity.

Table 3 Maximum difference R_s for the computation of N_q

	n	β(°)	Asso/Non-asso	Δ/B (%)	K_0	R_s (%)
Test6	1.0	N/A	Nsso	10.5	0.5	7.0
			Non-asso	12.5	0.5	6.6
			Asso	8	2.0	6.1
Test7	0.85	45	Asso	7.6	0.5	20.0
Test8	0.707	45	Asso	6	0.5	**28.3**
			Non-asso	7.6	0.5	24.4
			Asso	4.2	2.0	4.6
Test9	0.707	22.5	Asso	6.5	0.5	6.5
Test10	0.707	0	Asso	10	0.5	**3.4**

5. CONCLUSIONS

In this paper, a plane-strain elastic-perfectly-plastic non-coaxial soil model with an anisotropic yield criterion was applied to investigate smooth strip footing problems. Semi-analytical solutions of the bearing capacity for a smooth strip footing resting on an anisotropic, weightless, cohesive-frictional soil were developed based on the slip line method. Influences of the degree of soil anisotropy and non-coaxiality, on the bearing capacity of footing problems, were discussed. Based on the above analyses, the following conclusions can be drawn:

- The soil mass adjacent to the footing edge exhibited severe principal stress rotations.
- Without considering the non-coaxial plasticity (i.e., k=0.0), the numerical results were similar to the semi-analytical solutions, highlighting the capability of the numerical procedures and validation of the proposed model.
- The ultimate bearing capacity was much lower if soil yield anisotropy was involved. The exclusion of initial soil strength anisotropy tended to delay the onset of the ultimate bearing capacity N_c and N_q.
- Non-coaxial modelling affected the settlement prior to collapse, which indicated that the soil was softened. The degree of non-coaxial effects depended on the initial stress state,

the degree of initial strength anisotropy, and the flow rule. The ultimate bearing capacity was rarely affected by the inclusion of non-coaxial plasticity. It is necessary to consider both initial strength anisotropy and non-coaxiality when analyzing strip footing problems.

6 ACNOWLEDGEMENTS

This work was supported by the National Natural Science Foundation of China (Grant Nos. 51609204, 51608454, and 51408326); the State Key Laboratory for GeoMechanics and Deep Underground Engineering, China University of Mining and Technology (Grant No. SKLGDUEK1411); and the Fundamental Research Funds for the Central Universities (Grant Nos. 2682015CX092 and 2682016CX084).

APPENDIX 1

The matrix $\boldsymbol{N}$ can be written as follows:

$$\boldsymbol{N} = \begin{bmatrix} a & -a & b \\ -a & a & -b \\ c & -c & d \end{bmatrix} \quad \text{A.1}$$

The expressions for a, b, c and d are listed below:

$$\mathrm{a} = \mathrm{k} \cdot \mathrm{H} \cdot [-\frac{\sigma_{xy}}{4\sigma_{xy}^2 + (\sigma_x - \sigma_y)^2}] \quad \text{A.2}$$

$$\mathrm{b} = \mathrm{k} \cdot \mathrm{H} \cdot [\frac{\sigma_x - \sigma_y}{4\sigma_{xy}^2 + (\sigma_x - \sigma_y)^2}] \quad \text{A.3}$$

$$\mathrm{c} = \mathrm{k} \cdot \mathrm{I} \cdot [-\frac{\sigma_{xy}}{4\sigma_{xy}^2 + (\sigma_x - \sigma_y)^2}] \quad \text{A.4}$$

$$\mathrm{d} = \mathrm{k} \cdot \mathrm{I} \cdot [\frac{\sigma_x - \sigma_y}{4\sigma_{xy}^2 + (\sigma_x - \sigma_y)^2}] \quad \text{A.5}$$

where

$$\mathrm{H} = -2\sin(2\Theta + 2\mathrm{m}) \cdot (1 + \mathrm{m}_{\Theta}) \quad \text{A.6}$$

$$I = 2\cos(2\Theta+2m)\cdot(1+m_{\Theta}) \qquad \text{A.7}$$

For a rotational ellipse anisotropic yield criterion, the definition of m_{Θ} is written as follows:

$$m_{\Theta} = \frac{4(1-n^2)\cdot\cos(4\Theta-4\beta)\cdot C - 4D^2}{C^2} \qquad \text{A.8}$$

where

$$C = 2(n^2-1)\cos^2(2\Theta-2\beta)+2 \qquad \text{A.9}$$

$$D = (1-n^2)\sin(4\Theta-4\beta) \qquad \text{A.10}$$

APPENDIX 2

1. Governing equations of stresses

The two characteristics lines, i.e., α-lines and β-lines, are integrals of Equation (14) and Equation (15), respectively. Hence, the canonical form of the equilibrium equation can be written as follows:

$$\sin[2(m-\nu)]\frac{\partial p}{\partial\alpha} + 2F\frac{\partial\Theta}{\partial\alpha} + \gamma\cos(2m)\left[\sin(2\nu)\frac{\partial x}{\partial\alpha} + \cos(2\nu)\frac{\partial y}{\partial\alpha}\right] = 0 \qquad \text{A.11}$$

$$\sin[2(m+\nu)]\frac{\partial p}{\partial\beta} + 2F\frac{\partial\Theta}{\partial\beta} + \gamma\cos(2m)\left[-\sin(2\nu)\frac{\partial x}{\partial\beta} + \cos(2\nu)\frac{\partial y}{\partial\beta}\right] = 0 \qquad \text{A.12}$$

For a cohesive-frictional soil with no self-weight, γ is neglected. Then Equation A.11 and A.12 are reduced to the definitions shown below:

$$\sin[2(m-\nu)]\frac{\partial p}{\partial\alpha} + 2F\frac{\partial\Theta}{\partial\alpha} \qquad \text{A.13}$$

$$\sin[2(m+\nu)]\frac{\partial p}{\partial\alpha} + 2F\frac{\partial\Theta}{\partial\alpha} \qquad \text{A.14}$$

Which are hyperbolic if the characteristics defined in Equation (14) and Equation (15) are real and distinct.

Recalling the anisotropic yield criterion in Section 2.1, the variation of the stress state in an anisotropic plastic region can be shown as follows:

$$dp + (p + c\cot\phi_{max})\frac{2sin\phi(\Theta)}{sin2(m-\nu)}d\Theta = 0 \qquad \text{A.15}$$

$$dp + (p + c\cot\phi_{max})\frac{2sin\phi(\Theta)}{sin2(m+\nu)}d\Theta = 0 \qquad \text{A.16}$$

2. Stress boundary conditions

The normal and shear stresses at the boundary must lie on the Mohr circle that touches the failure envelope. For a strip footing problem with anisotropic soil mass, the shear stress acting on the boundary is zero. Following a geometrical calculation, the mean stress p can be solved as follows:

$$p = \frac{\sigma_n \mp c\cot\phi_{max} \sin\phi(\Theta)}{1 \pm \sin\phi(\Theta)} \quad \text{A.17}$$

where the first sign n=1.0 applies to the case in which σ_n is the major principal stress, and the second sign n=2.0 applies to the case in which it is the minor principal stress.

As shown in Fig. 8, the family of straight β-lines indicate the characteristics within the region OCD, which demonstrate an angle of Θ. The extent of the region OCD is governed by the condition that OA is smooth. In other words, $\Theta = 0^\circ$ on $\overline{OA}$. This statement implies that the angle ∠COD is a right angle. Hence, following Equation A.17, two stress variables (p_1, Θ_1) and (p_2, Θ_2) can be obtained. When the two stress variables are given, and assuming the two stress variables are located at two points along the same family of β-lines, we can write the expression of vertical pressure at plastic collapse:

$$q_t = (1+\sqrt{\frac{2}{M}} n\sin\phi_{max})(e^{\int_0^{\pi/2} G(\Theta)d\Theta} \cdot \frac{q\sqrt{M}+\sqrt{M}c\cot\phi_{max}}{\sqrt{M}-\sqrt{2}n\sin\phi_{max}}) - c\cot\phi_{max} \quad \text{A.18}$$

and:

$$G(\Theta) = \frac{2\sqrt{2}n\sin\phi_{max}(C^2+D^2)}{\sqrt{2n}\sin\phi_{max}\cdot D\cdot C+\sqrt{C^5+D^2\cdot C^3-2C^4(n\sin\phi_{max})^2}} \quad \text{A.19}$$

$$C = 2[(1-n^2)\sin^2(2\Theta-2\beta)+n^2] \quad \text{A.20}$$

$$D = (n^2-1)\sin(4\Theta-4\beta) \quad \text{A.21}$$

$$M = 2[(1-n^2)\sin^2(2\beta)+n^2] \quad \text{A.22}$$

where n and β are the shape parameters of the anisotropic yield criterion.

References

[1] Roscoe KH, Bassett RH, Cole ERL. Principal axes observed during simple shear of a sand. Proc Geotech Conf, Oslo. 1967; (1): 231-237.

[2] Arthur JRF, Chua KS, Dunstan T. Induced anisotropy in a sand. Géotechnique. 1977; 27(1):13-30.

[3] Cai YY. An experimental study of non-coaxial soil behaviour using hollow cylinder testing. PhD Thesis, University of Nottingham, 2010.

[4] Yang LT. Experimental study of soil anisotropy using hollow cylinder testing. PhD Thesis, University of Nottingham, 2013.

[5] Rodriguez NM, Lade PV. Non-coaxiality of strain increment and stress directions in cross-anisotropic sand. International Journal of Solids and Structures. 2014; 51(5):1103-1114.

[6] Yang LT, Li X, Yu HS, Wanatowski D. A laboratory study of anisotropic geomaterials incorporating recent micromechanical understanding. Acta Geotechnica. 2016; 11(5):1111-1129.

[7] Drescher A, De Jong GDJ. Photoelastic verification of a mechanical model for the flow of a granular material. Journal of the Mechanics and Physics of Solids. 1972; 20(5):337-340.

[8] Christoffersen J, Mehrabadi MM, Nemat-Nasser S. A micromechanical description of granular material behavior. Journal of applied mechanics. 1981; 48(2):339-344.

[9] Zhang L. The behaviour of granular material in pure shear, direct shear and simple shear. PhD Thesis, Aston University 2003.

[10] Jiang M, Yu HS. Application of discrete element method to geomechanics. Modern trends in geomechanics: Springer; 2006. (106): 241-269.

[11] Li X, Yu HS. Numerical investigation of granular material behaviour under rotational shear. Géotechnique. 2010; 60(5):381-394.

[12] Tejchman J, Wu W. Non‐coaxiality and stress–dilatancy rule in granular materials: FE investigation within micro‐polar hypoplasticity. International journal for numerical and analytical methods in geomechanics. 2009; 33(1):117-142.

[13] Hashiguchi K., Tsutsumi S. Shear band formation analysis in soils by the subloading surface model with tangential stress rate effect. International Journal of Plasticity. 2003; 19(10):1651-1677.

[14] Lashkari A, Latifi M. A non‐coaxial constitutive model for sand deformation under rotation of principal stress axes. International journal for numerical and analytical methods in geomechanics. 2008; 32(9):1051-1086.

[15] Yu HS. Non-coaxial theories of plasticity for granular materials. The 12th international conference of international association for computer methods and advances in geomechanics (IACMAG), Goa, India 2008. 361-377.

[16] Yang Y, Yu HS. A kinematic hardening soil model considering the principal stress rotation. International Journal for Numerical and Analytical Methods in Geomechanics. 2013; 37(13):2106-2134.

[17] Li XS, Dafalias YF. A constitutive framework for anisotropic sand including non-proportional loading. Géotechnique 2004; 54(1):41-55.

[18] Gao ZW, Zhao JD, Li XS Dafalias YF. A critical state sand plasticity model accounting for fabric evolution. International journal for numerical and analytical methods in geomechanics. 2014; 38(4):370-390.

[19] Gao ZW, Zhao JD. A non-coaxial critical-state model for sand accounting for fabric anisotropy and fabric evolution. International Journal of Solids and Structures. 2017; 106:200-212.

[20] Gräbe PJ, Clayton CR. Effects of principal stress rotation on permanent deformation in rail track foundations. Journal of Geotechnical and Geoenvironmental Engineering. 2009; 135(4):555-565.

[21] Bohnhoff M, Grosser H, Dresen G. Strain partitioning and stress rotation at the North Anatolian fault zone from aftershock focal mechanisms of the 1999 Izmit M w= 7.4 earthquake. Geophysical Journal International. 2006; 166(1):373-385.

[22] Yang Y, Yu HS. Application of a non-coaxial soil model in shallow foundations. Geomechanics and Geoengineering: An International Journal. 2006; 1(2):139-150.

[23] Yuan X. Non-coaxial plasticity for granular materials. PhD Thesis, University of Nottingham, 2005.

[24] Tsutsumi S, Hashiguchi K. General non-proportional loading behavior of soils. International Journal of Plasticity. 2005; 21(10):1941-1969.

[25] Davis EH, Christian JT. Bearing Capacity of Anisotropic Cohesive Soil. Journal of the Soil Mechanics and Foundations Division. 1971; 97(5):753-769.

[26] Abbo AJ. Finite element algorithms for elastoplasticity and consolidation. PhD Thesis, University of Newcastle Upon Tyne, 1997.

[27] Yu HS. Plasticity and Geotechnics: Springer US; 2006.

[28] Bishop JFW. On the complete solution to problems of deformation of a plastic-rigid material. Journal of the Mechanics and Physics of Solids. 1953; 2(1):43-53.

[29] Cox AD. Axially-symmetric plastic deformation in soils—II. Indentation of ponderable soils. International Journal of Mechanical Sciences. 1962; 4(5):371-380.

[30] Spencer AJM. Perturbation methods in plasticity—III plane strain of ideal soils and plastic solids with body forces. Journal of the Mechanics and Physics of Solids. 1962; 10(2):165-177.

[31] Chen, WF. Limit analysis and soil plasticity: Elsevier Scientific Pub. Co; 1975.